Life Metabolism, 2023, **Volume 2, Issue 6,** 266–279
https://doi.org/10.1093/lifemeta/load038
Advance access publication 27 September 2023
Original Article

Life
Metabolism

Mitochondrial YBX1 promotes cancer cell metastasis by inhibiting pyruvate uptake

Huan Chen[1,2], Ting Ling[1,2], Di Chen[1], Wenjuan Liu[1,2], Huan Qi[1], Tian Xia[1], Xiaolong Liu[1], Wen Wang[1], Xin Guo[1], Wuxiyar Otkur[1], Fangjun Wang[1,2], Zhaochao Xu[1,2], Jean-Claude Martinou[3], Hai-long Piao[1,2,*]

[1]CAS Key Laboratory of Separation Science for Analytical Chemistry, Dalian Institute of Chemical Physics, Chinese Academy of Sciences, Dalian, Liaoning 116023, China
[2]University of Chinese Academy of Sciences, Beijing 100049, China
[3]Department of Cell Biology, University of Geneva, 1211 Geneva, Switzerland

[*]Corresponding author. CAS Key Laboratory of Separation Science for Analytical Chemistry, Dalian Institute of Chemical Physics, Chinese Academy of Sciences, Lvshunzhonglu 568, Gaoxinqu, Dalian, Liaoning 116023, China. E-mail: hpiao@dicp.ac.cn

Abstract

Pyruvate is an essential fuel for maintaining the tricarboxylic acid (TCA) cycle in the mitochondria. However, the precise molecular mechanism of pyruvate uptake by mitochondrial pyruvate carrier (MPC) is largely unknown. Here, we report that the DNA/RNA-binding protein Y-box binding protein 1 (YBX1) is localized to the mitochondrial inter-membrane space by its C-terminal domain (CTD) in cancer cells. In mitochondria, YBX1 inhibits pyruvate uptake by associating with MPC1/2, thereby suppressing pyruvate-dependent TCA cycle flux. This association, in turn, promotes MPC-mediated glutaminolysis and histone lactylation. Our findings reveal that the YBX1-MPC axis exhibits a positive correlation with metastatic potential, while does not affect cell proliferation in both cultured cells and tumor xenografts. Therefore, the restricted pyruvate uptake into mitochondria potentially represents a hallmark of metastatic capacity, suggesting that the YBX1-MPC axis is a therapeutic target for combating cancer metastasis.

Keywords: mitochondria; YBX1; pyruvate metabolism; MPC1/2; metastasis

INTRODUCTION

Dysregulation of pyruvate metabolism is closely related to human diseases, including cancer, diabetes, and obesity [1, 2]. Pyruvate, the key metabolite mainly produced by glycolysis, is subsequently converted into lactate in the cytosol or transported into the mitochondria as a substrate for the tricarboxylic acid (TCA) cycle for further oxidation. Differentiated mammalian cells are mainly dependent on pyruvate oxidation to generate adenosine triphosphate (ATP) for free energy in cells. Highly proliferating cancer cells produce ATP, and biomass mainly relies on a high rate of glycolysis even under aerobic conditions [3]. In addition, pyruvate is mainly converted to lactate and cooperates with nicotinamide adenine dinucleotide (reduced form) (NADH) to regenerate nicotinamide adenine dinucleotide (NAD^+), which maintains NAD^+/NADH homeostasis and further promotes aerobic glycolysis [4]. However, pyruvate mitochondrial oxidation is conceptually simple but mechanistically complicated. Uncovering the mechanism of pyruvate mitochondrial oxidation has been a challenging problem. Mitochondrial pyruvate is oxidized to generate acetyl coenzyme A by the pyruvate dehydrogenase complex, which can be further converted into citrate, or converted into oxaloacetate by pyruvate carboxylase (PC).

The mitochondrial pyruvate carrier (MPC) complex is the only known pyruvate carrier in the inner mitochondrial membrane (IMM) [5, 6]. Hence, MPC activity not only determines mitochondrial pyruvate oxidation but is also associated with aerobic glycolysis [7–10]. Three homologous genes, *MPC1*, *MPC1L*, and *MPC2*, are involved in the mammalian genome in response to the MPC complex in cells [11, 12]. MPC1 and MPC2 are widely expressed in different tissues and cells, whereas MPC1L is only found in the fetal heart and cells involved in the process of spermiogenesis [11]. In most mammalian cells, the functional MPC complex is composed of MPC1–MPC2 heterodimer [13], and loss of expression of either one will disrupt the activity of this complex and lead to the degradation of the other one [12]. Because cancer cells are dependent on aerobic glycolysis for rapid cell proliferation, loss of MPC expression or inhibition of MPC activity promotes cancer initiation [14] and progression [7, 10, 15].

Y-box binding protein 1 (YBX1) is a canonical DNA/RNA-binding protein that regulates transcription, translation, and RNA splicing as well as stabilization [16–19], and its loss of expression leads to late-stage embryonic development failure in mice [20]. YBX1 has been intensively studied in cancer progression, invasion, and metastasis [18, 21, 22]. Recently, a study showed that the expression of YBX1 is upregulated in white adipose tissue under cold exposure, which enhances mouse adaptation to cold temperatures by promoting adipocyte differentiation and oxygen consumption rate (OCR) [23]. In addition, YBX1 induces aerobic glycolysis by activating the protein expression of hypoxia-inducible factor 1α (HIF1α) and MYC (v-myc avian myelocytomatosis viral oncogene homolog, cellular myelocytomatosis viral oncogene homolog [c-MYC]) in gastric cancer cells [24]. Here, we uncover

Received 6 September 2023; revised 20 September 2023; accepted 26 September 2023.

previously undescribed YBX1 mitochondrial function and identified YBX1 as a suppressor for MPC for cancer metastasis.

RESULTS

YBX1 resides in the mitochondrial inter-membrane space

Previously, several studies demonstrated that YBX1 is associated with mitochondria [25–27], and numerous mitochondrial proteins interact with YBX1 [28, 29]. To explore the potential role of YBX1 in mitochondria, we first examined the authenticity of YBX1's mitochondrial localization. We found that a portion of YBX1 colocalized with the mitochondrial marker pyruvate dehydrogenase E1 subunit alpha 1 (PDHA1) in several cell lines (Fig. 1a; Supplementary Fig. S1a). In contrast, Ybx1 showed minimal mitochondrial localization in mouse embryonic fibroblast (MEF) cells (Supplementary Fig. S1b). This phenomenon was also confirmed with the subcellular fractionation assay of YBX1 by using western blot analysis (Fig. 1b; Supplementary Fig. S1c).

As the submitochondrial distribution of YBX1 is still debatable [25–27] and the functions of mitochondrial proteins are compartmentalized based on their location, we performed proteinase K (PK) digestion assays to further examine the submitochondrial localization of YBX1. We found that a fraction of YBX1 was digested by PK, but the remaining part of YBX1 was protected from PK digestion (Fig. 1c; Supplementary Fig. S1d). Furthermore, YBX1 protein was entirely digested when the outer mitochondrial membrane (OMM) was disrupted (Fig. 1c; Supplementary Fig. 1d), indicating exposure of YBX1 to the mitochondrial inter-membrane space (IMS). In addition, we found that YBX1 was highly extracted by sodium carbonate (pH 11.5) and sonication (Supplementary Fig. S1e), which indicated that YBX1 is not an inherent IMM protein. Subsequently, upon treating the mitochondria with sequentially increasing strengths of sodium carbonate, a fraction of YBX1 in mitochondria showed tight membrane-bound properties (Fig. 1d), similar to the well-known membrane-bound proteins succinate dehydrogenase complex subunit A (SDHA) and apoptosis-inducing factor. Moreover, despite washing the extracted mitochondria twice with the isolation buffer, a small portion of YBX1 was still present in the supernatant of intact mitochondria (Fig. 1d; Supplementary Fig. S1e), indicating its loose association with the OMM, which is consistent with the previous reports [26, 27]. Finally, we utilized immune-electron microscopy (Immuno-EM) to confirm the mitochondrial localization of YBX1. Before Immuno-EM assay, the examination conditions of the YBX1 antibody were pre-confirmed by immunofluorescence staining (Supplementary Fig. S1f, left panel). We observed that the gold-labeled YBX1 was localized to the mitochondria in both control MDA-MB-231 cells and its isolated mitochondria (Fig. 1e; Supplementary Fig. S1f, right panel).

Most mitochondrial proteins are targeted to the mitochondria via N-terminal mitochondrial targeting sequences (MTS). However, we did not observe the MTS in the YBX1 protein sequence. Indeed, the N-terminal truncated YBX1 did not destroy the mitochondrial localization of YBX1 (Supplementary Fig. S1g and h). To map the mitochondrial targeting amino acid sequences of YBX1, we constructed several S protein-Flag-Streptavidin binding peptide (SFB)-tagged truncated YBX1 and examined its subcellular localization. Interestingly, the YBX1 C-terminal domain (CTD) was predominantly localized to the nucleus (Fig. 1f and g), which is consistent with a previous report [30], however, the CTD was also crucial for YBX1 mitochondrial localization (Fig. 1f and g).

We also tested the CTD localization in MEFs to understand the conditions under which YBX1 targets mitochondria. The CTD in MEFs was exclusively localized to the nucleus (Supplementary Fig. S1i), in contrast to its localization in MDA-MB-231 cells. Collectively, these findings suggested that YBX1 is imported to the mitochondrial IMS via its CTD.

YBX1 inhibits mitochondrial pyruvate uptake in cancer cells

Next, to identify potential interacting proteins of mitochondrial YBX1, we performed an immunoprecipitation-mass spectrometry (IP-MS) assay in the isolated mitochondria from SFB-YBX1 transduced HEK293T cells. In total, we identified 17 mitochondrial proteins compared to the control cells (Supplementary Fig. S2a). Among them, several potential interactors are mitochondrial tRNA ligase, consistent with YBX1 binding to various mitochondrial tRNAs [26]. In addition, we observed the high-ranking presence of MPC1 and MPC2 in our assay (Supplementary Fig. S2a). Since MPC1 and MPC2 are implicated in mitochondrial pyruvate uptake [5, 6], thereby regulating the TCA cycle, and fluctuations in the levels of intermediates within the TCA cycle dictate physiology and cell fate, we have decided to validate the potential interactions between MPC1/2 and YBX1.

We first determined the interplay between YBX1 and MPC activity. The downregulation of *YBX1* increased pyruvate uptake into mitochondria, however did not affect MPC1/2 expression (Fig. 2a and b; Supplementary Fig. S2b). Using metabolic flux analysis, we observed that [U-^{13}C] glucose-labeled citrate and the ratio of labeled [$^{13}C_2$] citrate to [$^{13}C_3$] pyruvate increased in *YBX1* knockdown MDA-MB-231 cells (Fig. 2c and d). In addition, YBX1 inactivation increased citrate levels and the maximum OCR and reduced the levels of pyruvate and lactate (Fig. 2e and f). Moreover, we observed similar results in the HEK293T cells (Supplementary Fig. S2c–e), a cell line with a high rate of glycolysis [31, 32]. We also explored the labeling in [$^{13}C_3$] alanine, [$^{13}C_3$] aspartic acid, and [$^{13}C_3$] citrate to verify the flux of pyruvate entering into the mitochondria (Supplementary Fig. S2f). The ratio of [$^{13}C_3$] alanine/[$^{13}C_3$] pyruvate, a proxy for mitochondrial pyruvate uptake [33], was increased in *YBX1* knockdown MDA-MB-231 cells (Fig. 2g). Moreover, the ratios of [$^{13}C_3$] aspartic acid/[$^{13}C_3$] pyruvate and [$^{13}C_3$] citrate/[$^{13}C_3$] pyruvate, which indicate the PC-dependent pyruvate flux, were elevated in *YBX1* knockdown MDA-MB-231 cells (Supplementary Fig. S2g and h). However, these ratios were not changed in *Ybx1* knockout (*Ybx1*$^{-/-}$) MEF cells (Supplementary Fig. S2i–k), consistent with a sparse mitochondrial localization of Ybx1. We next examined the effect of YBX1 on MPC by performing [U-^{13}C] pyruvate metabolic flux analysis. Consistently, *YBX1* knockdown increased [U-^{13}C] pyruvate-traced citrate and the ratio of labeled [$^{13}C_2$] citrate to [$^{13}C_3$] pyruvate in MDA-MB-231 cells (Fig. 2h and i). Furthermore, [U-^{13}C] pyruvate-traced citrate levels were increased in several different cancer cell lines by downregulation of *YBX1* (Supplementary Fig. S2l), which implied that this phenomenon is ubiquitous among cancer cells.

Next, we performed reconstitution experiments by restoring YBX1 expression in *YBX1* knockout (*YBX1*$^{-/-}$) MDA-MB-231 cells (Supplementary Fig. S2m). Restoration of YBX1 rescued the decreased [U-^{13}C] pyruvate-labeled citrate in *YBX1*$^{-/-}$ MDA-MB-231 cells (Fig. 2j). In addition, the MPC inhibitor UK5099 or knockout of *MPC1* completely abolished the regulatory function of YBX1 in flux of pyruvate in TCA cycle (Fig. 2j and l; Supplementary Fig. S2n). Moreover, in *YBX1* knockdown cells, UK5099 almost completely inhibited the elevated maximum OCR (Fig. 2m; Supplementary

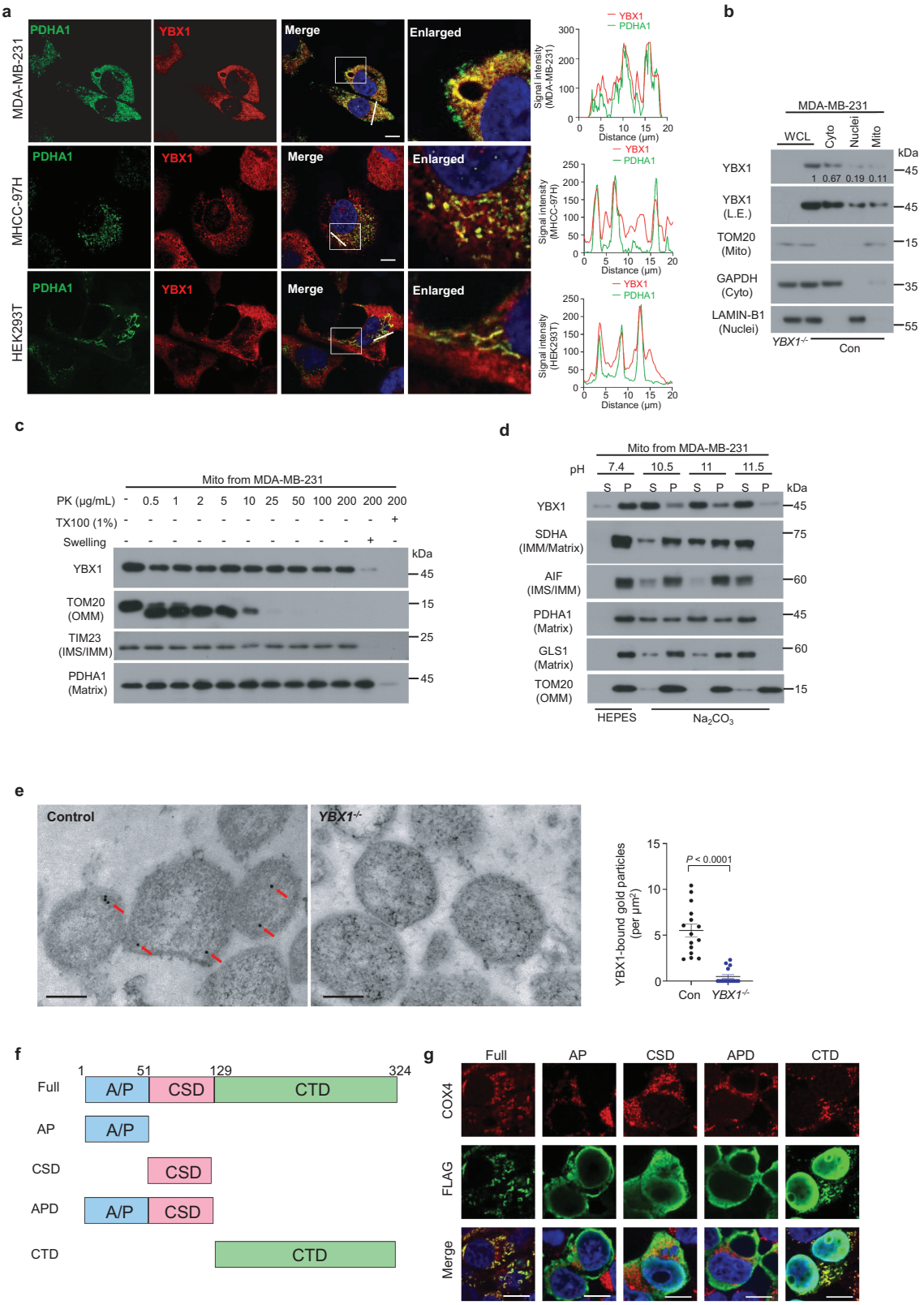

Figure 1 YBX1 resides in the mitochondrial IMS. (a) Representative images of colocalization of YBX1 and PDHA1 in MDA-MB-231, MHCC-97H, and HEK293T cells. Red indicates YBX1 and green indicates PDHA1. Scale bar, 10 μm. (b) Immunoblotting analysis of subcellular distribution of YBX1. Cytosol (Cyto), the supernatant in isolated mitochondria (Mito) described in the methods. GAPDH, a cytosol protein; LAMIN-B1, a nuclear protein; TOM20, a mitochondrial protein. (c) Immunoblotting analysis of submitochondrial YBX1 using PK assays in MDA-MB-231 cells. TX100, Triton-X 100. TOM20, an OMM protein. TIM23, an IMM protein. PDHA1, a mitochondrial matrix protein. (d) Extraction of YBX1 in the isolated mitochondria from MDA-MB-231 cells using sodium carbonate (pH 10.5, 11, and 11.5) or isolation buffer. S, supernatant; P, pellet. (e) Immuno-EM analysis of gold-bound YBX1 in the isolated mitochondria from Control and YBX1$^{-/-}$ MDA-MB-231 cells. The data were obtained from random 15 images. Red arrows point to gold-bound YBX1. Scale bars, 200 nm. (f) Schematic representations of the full-length and truncated YBX1 constructs with AP (alanine/proline-rich domain), CSD, APD, and

Fig. S2o). These results demonstrate that YBX1 inhibits mitochondrial pyruvate uptake.

YBX1 inhibits mitochondrial pyruvate uptake by interacting with MPC

We next investigated the interaction between YBX1 and the MPC complex. In line with our IP-MS results, MPC1/2 and YBX1 form a complex in isolated mitochondria in MYC-MPC1/2 or MYC-YBX1 transduced HEK293T cells (Supplementary Fig. S3a). In addition, YBX1 was present in endogenous MPC1 immunoprecipitates in isolated mitochondria from HEK293T, MDA-MB-231, and MHCC-97H cells (Fig. 3a). Furthermore, MPC1/2 could be detected in endogenous YBX1 immunoprecipitates from HEK293T cells (Supplementary Fig. S3b). Finally, analysis of MPC-YBX1 complex via immunoprecipitation by FLAG-tagged MPC1 on blue native gels demonstrated that YBX1 associates with MPC1/2 complex (Supplementary Fig. S3c). Moreover, YBX1 significantly colocalized with MPC1/2 in MDA-MB-231 control cells, but not in *YBX1*$^{-/-}$ cells (Fig. 3b). To further examine the colocalization of YBX1 and MPC1/2 at the nanometer scale *in vivo*, we performed a structured illuminate microscopy (SIM) assay, and found that YBX1 showed strong colocalization with MPC1/2 (Fig. 3c; Supplementary Fig. S3d). Although the CTD is important to YBX1 mitochondrial localization (Fig. 2g), the cold shock domain (CSD) is necessary for the interaction with MPC1/2 (Fig. 3d). These results indicate that mitochondrial YBX1 associates with MPC1/2 through the CSD region.

To further verify the inhibitory mechanism of YBX1 in MPC activity, we performed a bioluminescence resonance energy transfer (BRET)-based REporter Sensitive to PYRuvate (RESPYR) system assay [13]. MPC undergoes conformational changes upon binding to its substrate pyruvate, increasing the energy resonance transfer in the RESPYR system [13]. Interestingly, the basal BRET signal was elevated in *YBX1* knockdown cells, and this elevation was increased upon pyruvate treatment (Fig. 3e, Supplementary Fig. S3e and f). However, YBX1 inactivation did not alter the sensitivity of MPC1/2 to pyruvate in the RESPYR system (Supplementary Fig. S3g). Moreover, the interaction between MPC1 and MPC2 was increased in *YBX1* knockdown cells (Fig. 3f), and this interaction was increased in the presence of pyruvate (Supplementary Fig. S3h). Therefore, YBX1 associates with MPC1/2 and inhibits its pyruvate transport activity.

YBX1 reprograms cancer cell metabolism by modulating MPC activity

Glutaminolysis is a hallmark of cancer metabolism [34, 35] and is enhanced by MPC activity inhibition [36, 37]. Subsequently, UK5099 treatment increased the [U-^{13}C] glutamine-traced citrate (M+3, M+4, M+5, and M+6) as well as M+5 glutamate and α-ketoglutarate (α-KG) (Fig. 4a–c). c-MYC is a well-known regulatory factor for glutaminolysis [38, 39], and has been shown to be increased by YBX1 expression in hematological malignant cancers [40–42]. In addition, another study demonstrated that inactivation of YBX1 reduces the mRNA stability of c-MYC [40]. However, knockdown of *YBX1* did not affect protein levels of c-MYC in MDA-MB-231 cells (Fig. 4d). To exclude cell line specificity, we knocked down YBX1 expression in a panel of cell lines. Indeed, the inactivation of YBX1 reduced c-MYC expression in MHCC-97H, HBE (human bronchial epithelial), and SUM159 cells; however, c-MYC expression was not altered in HEK293T, MCF-10A, and T47D cells (Supplementary Fig. S4a). In addition, glutaminase 1 (GLS1), a known c-MYC target gene, was not responsive to c-MYC protein alteration (Fig. 4d and e; Supplementary Fig. S4a), which is consistent with a previous report [43]. Nevertheless, the [U-^{13}C] glutamine-traced citrate, glutamate, and α-KG levels demonstrated that YBX1 and c-MYC independently regulate glutaminolysis (Fig. 4f and g; Supplementary Fig. S4b). Next, we used respiration buffer (with unlabeled malate but without glutamine) to perform [U-^{13}C] pyruvate tracing analysis in isolated mitochondria. We found that the labeling rate of citrate from [U-^{13}C] pyruvate was faster in the mitochondria of *YBX1* knockdown cells than in control cells (Fig. 4h). Instead of continuous accumulation, the M+3 isotopologues of pyruvate increased shortly and remained stable throughout the experiment (Fig. 4i). Notably, the levels of M+3 isotopologues of pyruvate and [U-^{13}C] pyruvate-traced citrate and malate were increased in the mitochondria of *YBX1* knockdown cells (Fig. 4i; Supplementary Fig. S4c). Furthermore, although glutamine deprivation elevated the flux from pyruvate to citrate, [U-^{13}C] pyruvate-traced citrate increased in *YBX1*-downregulated cells (Fig. 4j). Interestingly, [U-^{13}C] pyruvate-labeled citrate was markedly decreased by glutaminase inhibitor CB-839 treatment. However, YBX1 inactivation still promoted the enrichment of citrate labeling under glutaminolysis-inhibiting conditions (Supplementary Fig. S4d).

Inhibition of the MPC complex reduces mitochondrial pyruvate oxidation but promotes lactate production, which is the signature of cancer cells [9, 10]. Consistently, YBX1 inactivation did not reduce [U-^{13}C] glucose-traced pyruvate in *MPC1* knockout (*MPC1*$^{-/-}$) cells (Fig. 4k), indicating that the reduced pyruvate M+3 upon YBX1 inactivation is caused by MPC activation. In addition, labeled M+3 lactate was increased by *YBX1* downregulation in *MPC1* deletion cells (Supplementary Fig. S4e). Indeed, histone lactylation was decreased upon *YBX1* downregulation but restored by the MPC inhibitor UK5099 (Fig. 4l; Supplementary Fig. S4f) [44, 45]. Taken together, YBX1 reprograms cancer cell metabolism via MPC complex inhibition.

YBX1 promotes cancer cell metastasis by inhibiting the MPC complex

To further characterize the role of the YBX-MPC axis in cancer progression, we subcutaneously implanted *YBX1*-depleted MHCC-97H cells with or without *MPC1* short-hairpin RNA (shRNA) expression into nude mice. We observed that the mice implanted with *YBX1* knockdown cells showed smaller tumor volumes than the mice implanted with control cells. However, downregulation of *MPC1* in *YBX1* knockdown cells resulted in similar tumor volumes to *YBX1* knockdown cells (Fig. 5a; Supplementary Fig. S5a and b). Moreover, the knockdown of *YBX1* decreased cell growth; however, the MPC inhibitor UK5099 did not rescue the decreased cell proliferation in *YBX1*-downregulated cells (Supplementary Fig. S5c and d). In addition, different concentrations of UK5099 did not influence the cell growth rate in several different cell lines (Fig. 5b and c).

Next, we found that knockdown of *YBX1* reduced cell invasion, and this reduction was partly restored by MPC complex

CTD regions. (g) Representative images of colocalization of SFB-tagged truncated YBX1 and cytochrome c oxidase subunit 4 (COX4) in HEK293T cells. Red indicates COX4 and green indicates FLAG. Scale bars, 10 μm. Results in the right panel of (e) are the mean of biological replicates from a representative experiment, and error bars indicate standard error of the mean (SEM). Statistical significance was determined by a two-tailed, unpaired Student's *t*-test. All other experiments were repeated independently at least three times.

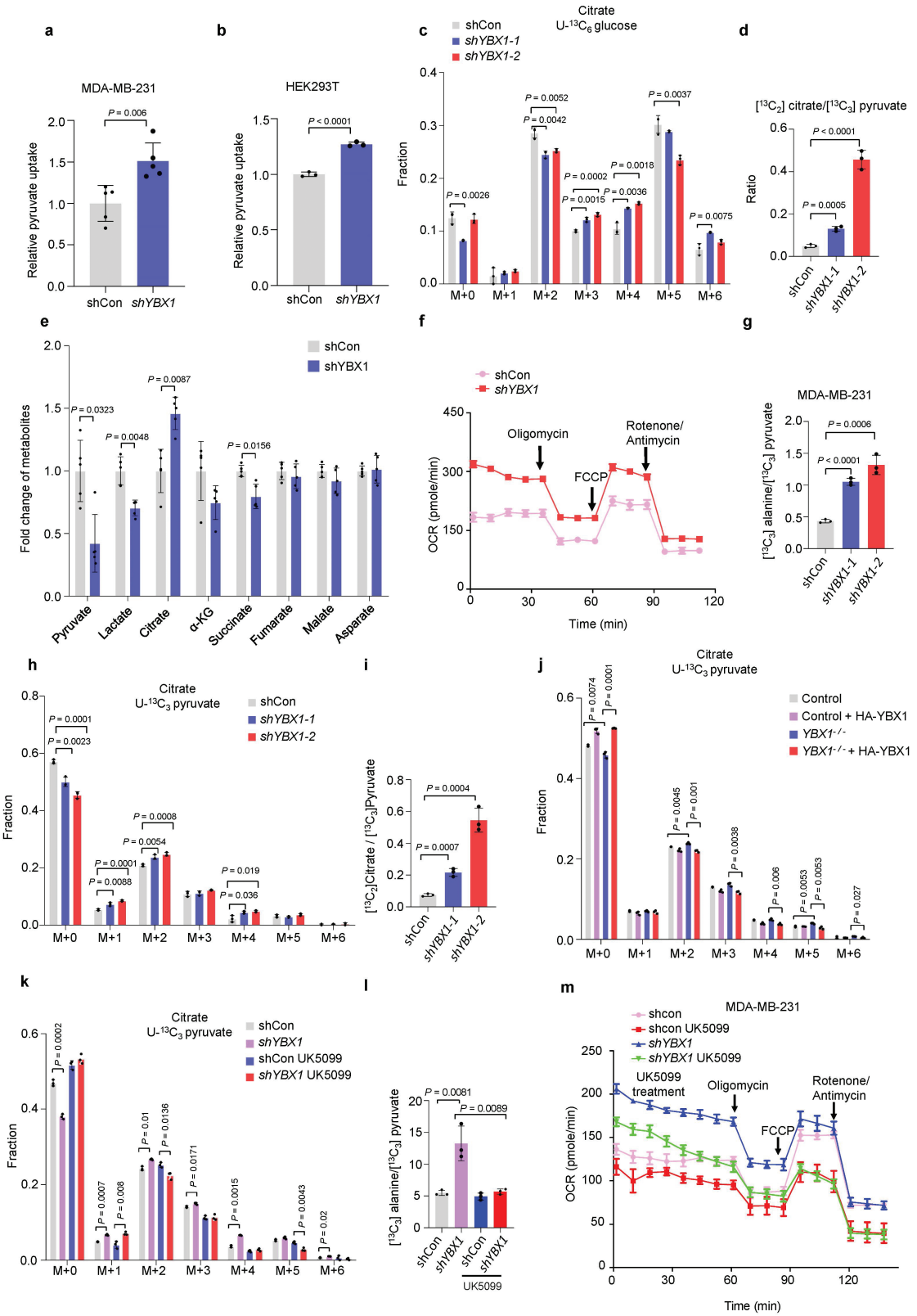

Figure 2 YBX1 inhibits mitochondrial pyruvate uptake in cancer cells. (a and b) Pyruvate uptake into mitochondria in cells transfected with control and *YBX1* shRNA in MDA-MB-231 cells ($n = 5$ biological independent samples) (a), and HEK-293T cells ($n = 3$ biological independent samples) (b). (c and d) Mass isotopologue analysis of citrate in control and *YBX1* knockdown MDA-MB-231 cells incubated with [U-^{13}C] glucose (c), and the ratio of [$^{13}C_2$] citrate/[$^{13}C_3$] pyruvate from (c) ($n = 3$ biological independent samples) (d). (e–g) Analysis of TCA cycle intermediate levels ($n = 5$ biological independent samples) (c), measurement of OCR ($n = 4$ biological independent samples) (d), and the ratio of [$^{13}C_3$] alanine/[$^{13}C_3$] pyruvate from [U-^{13}C] glucose tracing ($n = 3$ biological independent samples) (e) in MDA-MB-231 cells transduced with control and *YBX1* shRNA. (h and i) Mass isotopologue analysis of citrate in control and *YBX1* knockdown MDA-MB-231 cells incubated with [U-^{13}C] pyruvate (h), and the ratio of [$^{13}C_2$] citrate/[$^{13}C_3$] pyruvate from (h) ($n = 3$ biological independent samples) (i). (j) Mass isotopologue analysis of citrate in control and *YBX1*$^{-/-}$ MDA-MB-231 cells transduced with HA-YBX1 and incubated

inhibition (Fig. 5d). Moreover, *YBX1* knockdown cells had fewer lung metastatic nodules than those injected with control cells (Fig. 5e–g). However, knockdown of *MPC1* resulted in more lung metastatic nodules than control injected cells, and inhibition of MPC1 increased the metastatic nodules in *YBX1* knockdown cells (Fig. 5e–g). Both YBX1 and MPC are closely related to epithelial-to-mesenchymal transition (EMT) [16, 22, 46–48], which contributes to metastasis. Nevertheless, MPC inhibition did not affect EMT markers in either control or *YBX1* knockdown cells (Supplementary Fig. S5e). To investigate the relevance of our findings in human cancer, we evaluated the prognostic value of YBX1, MPC1, and MPC2 in a cancer dataset. Notably, patients with high levels of YBX1 exhibited shorter distant metastasis-free survival and relapse-free survival (Fig. 5h; Supplementary Fig. S5f). In addition, the patients with high MPC2 levels had much longer distant metastasis-free survival but not relapse-free survival (Fig. 5h; Supplementary Fig. S5f). Taken together, these data demonstrate that YBX1 promotes cancer metastasis by inhibiting the MPC complex.

DISCUSSION

Previous studies have demonstrated that YBX1 has multiple roles in metabolic regulation, including suppressing oxidative phosphorylation [49], promoting aerobic glycolysis [24], and regulating adipocyte cold temperature adaptation [23]. In the present study, we demonstrate that YBX1 is not only associated with OMM [26, 27] but also imported to the mitochondrial IMS via its CTD. Of note, in cancer cells, YBX1 binds to MPC1/2 and inhibits mitochondrial pyruvate uptake, eventually reducing mitochondrial pyruvate oxidation and alanine production. However, we observed almost negligible mitochondrial localization of Ybx1 in MEF cells, indicating that an unknown mechanism mediates its mitochondrial localization, and this may be the reason why YBX1 is not included in MitoCorta 3.0 [50].

MPC1/2 are MPCs that were recently identified by two groups [5, 6], and they determine the rates of metabolic processes that rely on the pyruvate as a primary substrate, notably including the TCA cycle and pyruvate-to-alanine transition. In addition, inactivation of MPC activity enhances pyruvate conversion into lactate, thus promoting glutamine catabolism [36, 37], and associates with tumor initiation, metastasis, and poor prognosis [14, 46, 47]. Moreover, patients with high levels of lactate and pyruvate in serum exhibit increased metastatic capacity [51]. This study uncovered that YBX1 regulating pyruvate metabolism contributed to cancer metastasis, and MPC inhibition significantly increased lactate accumulation, histone lactylation, and metastatic nodules in *YBX1*-depleted cells. YBX1 contributes to metastasis by increasing HIF1α expression [18] and promoting EMT transition in cancer cells [16, 22, 48]. In addition, previous studies demonstrated that MPC inhibition promotes cancer metastasis by inducing EMT [46, 47]; however, we did not observe alterations of EMT marker protein in the present study by inhibiting MPC activity. Nevertheless, our results demonstrate that YBX1-mediated MPC inhibition reprograms lactate and glutamine metabolism, and these metabolic alterations are closely associated with increased cell invasion and metastasis [52–56].

YBX1 was initially documented to be localized within the mitochondria [25], where it functions as a mitochondrial DNA mismatch binding protein. However, two distinct research groups demonstrated that YBX1 was merely associated with the OMM [26, 27], as it failed to withstand the digestion by PK. One possibility is that mitochondria become swell and leaky, as the outer membrane may be broken when mitochondria were isolated by gradient centrifugation at a high speed [57]. An alternative possibility is that YBX1 binds to the OMM, where it is readily imported into the mitochondria under specific stress. Our results do not support that YBX1 localizes to the mitochondrial matrix, while YBX1 is implicated in mitochondrial DNA repair under thymidine-induced mitochondrial DNA damage [25] and *Helicobacter pylori* infection [58]. While our results do indicate a significant translocation of YBX1 to the mitochondrial IMS, where it regulates mitochondrial pyruvate metabolism by interacting with the MPC complex in cancer cells (a phenomenon that may extend beyond cancer cells, for instance, in HEK293T cells), the precise mechanism for these observations remains unresolved within the scope of our current study.

Materials and methods

Cell culture, transfection, and lentivirus production

Ybx1$^{-/-}$ MEFs were generated from *Ybx1*$^{fl/fl}$ mice and immortalized with simian virus 40 large-T (SV40 T) antigen using lentivirus transfection expressing Cre recombinase. MEFs, HEK293T, MDA-MB-231, HCCLM3, HBE, and MCF-7 cells were cultured in Dulbecco's modified Eagle's medium (DMEM) with 10% fetal bovine serum (FBS). SUM159PT, T47D, and MHCC-97H cells were cultured in RPMI1640 with 10% FBS. MCF-10A cells were cultured in DMEM with 5% FBS, 20 ng/mL epidermal growth factor, 10 μg/mL insulin, 0.5 μg/mL hydrocortisone, 100 ng/mL cholera toxin. HEK293T cells were transfected using polyethylenimine (PEI). The transfection mass ratio of plasmids to PEI was 1:3. Lentivirus production was performed using two systems. For the two-plasmid packaging system, psPAX2 and pVSVg together with targeting plasmids were cotransfected into HEK293T cells for 48 h to harvest the supernatant of lentivirus. For the three-plasmid packaging system, pMDLg, pVSVg, and pREV were used. Targeting cells were incubated with the medium mixed with the indicated supernatant of lentivirus for 24 h. Next, the cells were kept in the normal culture medium and used for further treatment.

CRISPR-Cas9 knockout of *YBX1* and *MPC1*

Single guide RNA (sgRNA) targeting sequences were designed using the online tool CHOPCHOP. Targeting sequences for *YBX1* were 5′-GTTCCCAAAACCTTCGTTGC-3′ and 5′-GTTTTCTTTTCCAGCAACGA-3′, and those for *MPC1* were 5′-GTTCCGAGGCTGTACCTTGT-3′ and 5′-GGGCTACTTCATTTGTTGCG-3′. The targeting sequences were inserted into the LentiCRISPR v2 vector. After infection, MDA-MB-231 cells were screened using puromycin

with [U-^{13}C] pyruvate (n = 3 biological independent samples). (k and l) Mass isotopologue analysis of citrate in MDA-MB-231 cells transduced with *YBX1* shRNA and incubated with [U-^{13}C] pyruvate under 20 μmol/L UK5099 treatment (n = 3 biological independent samples) (k), and the ratio of [$^{13}C_3$] alanine/[$^{13}C_3$] pyruvate from (k) (n = 3 biological independent samples) (l). (m) Measurement of OCR in control and *YBX1* knockdown MDA-MB-231 cells with or without UK5099 treatment (20 μmol/L) (n = 3 biological independent samples). Results are the mean of biological replicates from a representative experiment, and error bars indicate standard deviation (SD). Statistical significance was determined by a two-tailed, unpaired Student's t-test. All other experiments were repeated independently at least three times.

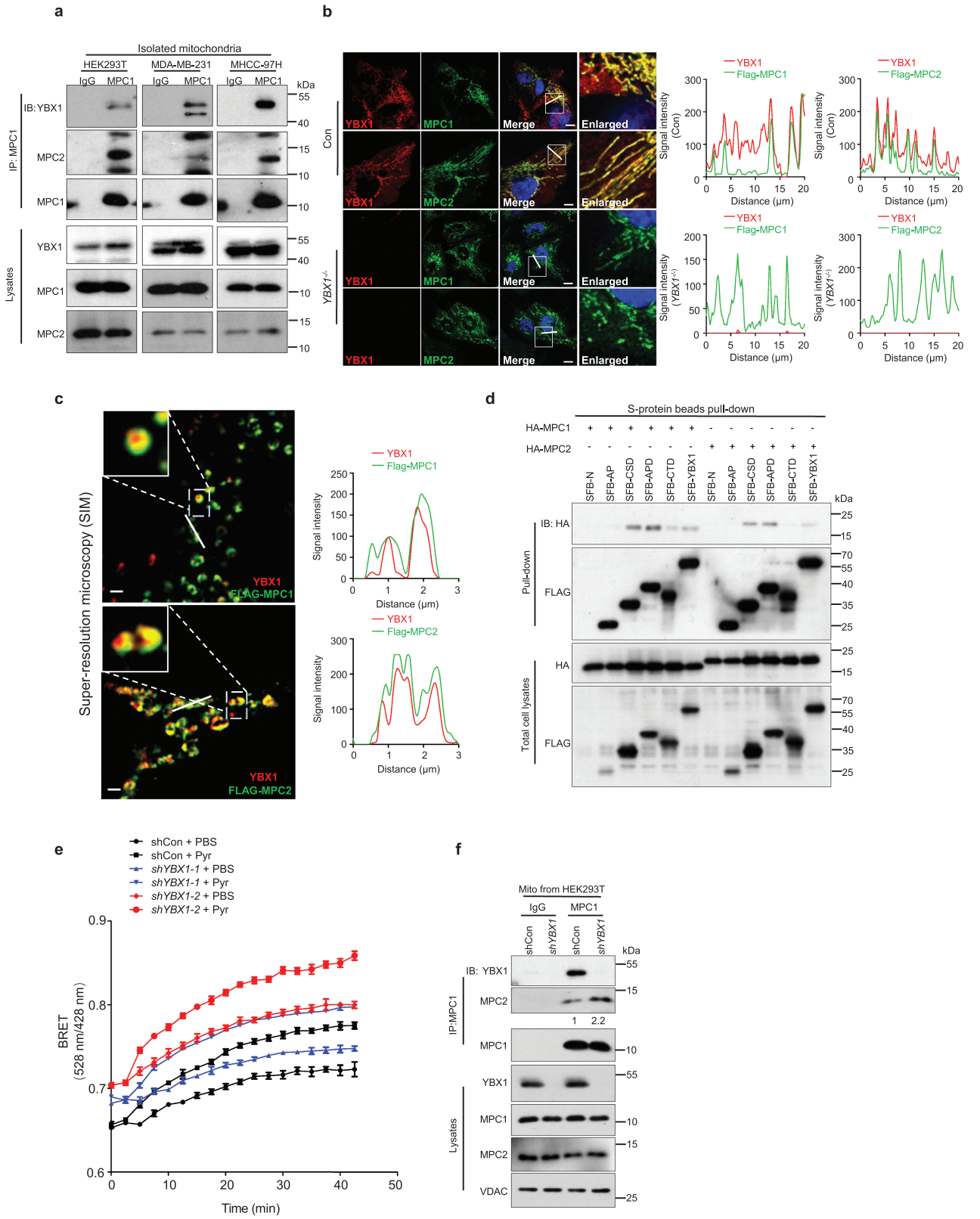

Figure 3 YBX1 inhibits mitochondrial pyruvate uptake by interacting with MPC. (a) MPC1 was immunoprecipitated in mitochondrial fractions from HEK293T, MDA-MB-231, and MHCC-97H cells, and immunoblotted with indicated antibodies. (b) Immunofluorescence analysis of YBX1 and FLAG-tagged MPC1/2 in control and *YBX1*$^{-/-}$ MDA-MB-231 cells. Red indicates YBX1 and green indicates FLAG. Scale bars, 10 μm. (c) SIM image analysis of YBX1 and MPC1/2 in HEK293T cells. Red indicates YBX1 and green indicates MPC1/2. Scale bars, 1 μm. (d) HEK293T cells were cotransfected with indicated plasmids and cell lysates were subjected to pulldown with S protein beads and immunoblotted with antibodies against FLAG and HA. (e) BRET kinetic analysis in control or *YBX1* knockdown HEK293T cells transfected MPC1-Venus and MPC2-Rluc reporters (n = 5). Pyr, 5 mmol/L pyruvate. Data are the mean of biological replicates from a representative experiment, and error bars indicate SEM. Statistical significance was determined by a two-tailed, unpaired Student's t-test. The experiments were repeated three times. (f) MPC1 was immunoprecipitated in mitochondria fractions from control shRNA and *YBX1* knockdown HEK293T cells and immunoblotted with indicated antibodies. All experiments were repeated independently at least three times.

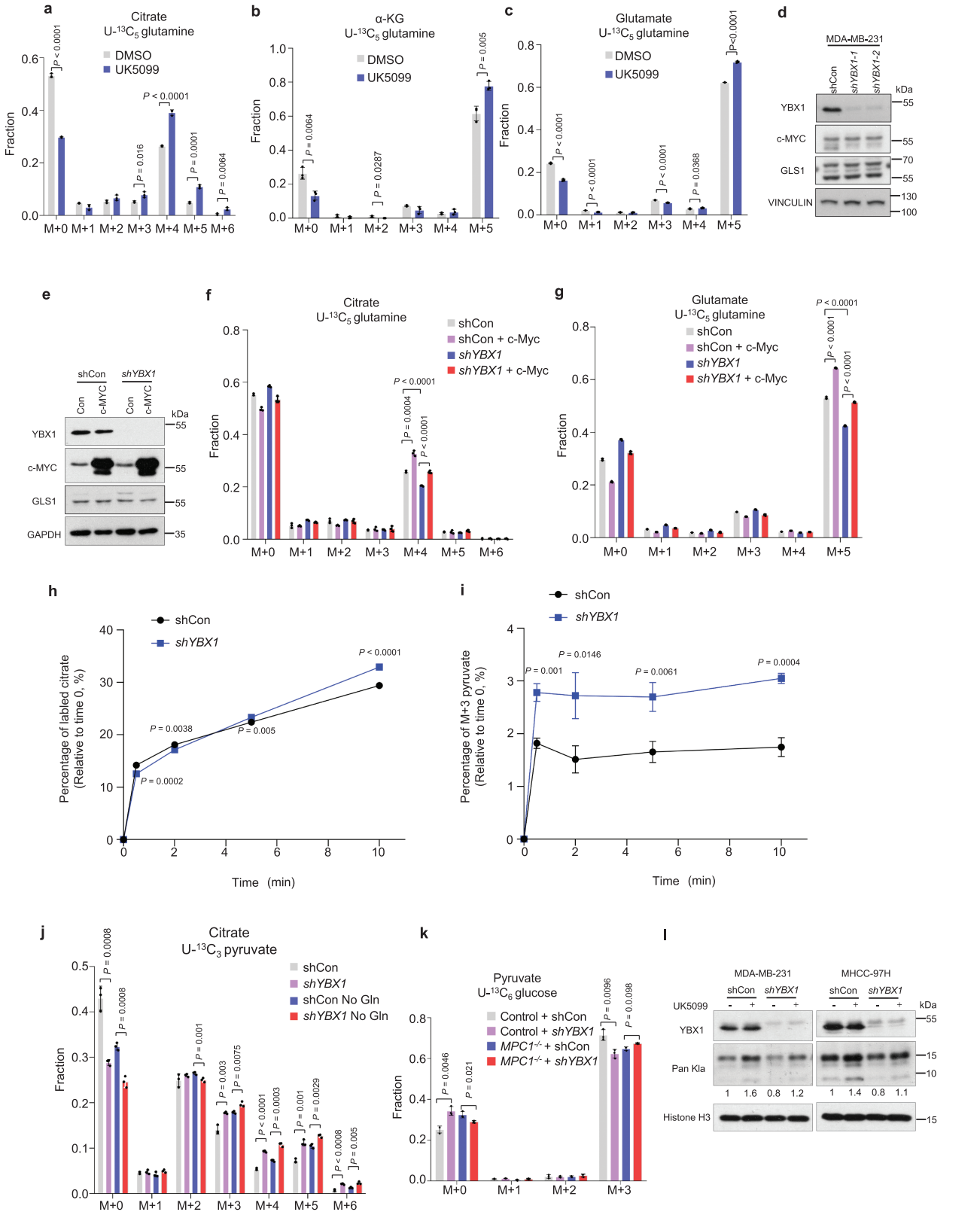

Figure 4 YBX1 reprograms cancer cell metabolism by modulating MPC activity. (a–c) Mass isotopologue analysis of citrate (a), α-KG (b), and glutamate (c) in MDA-MB-231 cells under UK5099 treatment and incubated with [U-^{13}C] glutamine (n = 3 biological independent samples). (d) Immunoblotting analysis of YBX1, c-MYC, GLS1, and VINCULIN in MDA-MB-231 cells. (e) Immunoblotting of YBX1, c-MYC, GLS1, and GAPDH in MDA-MB-231 cells transduced with control and *YBX1* shRNA or in combination with c-MYC expression vector. (f and g) Analysis of fraction enrichment of citrate (f) and glutamate (g) in cells from (e) incubated with [U-^{13}C] glutamine (n = 3 biological independent samples). (h and i) [U-^{13}C] pyruvate was incubated with isolated mitochondria fractions from control and *YBX1* knockdown HEK293T cells, and labeled citrates at different time points were present by subtracting the level at 0-time point (h), and the relative level of M+3 pyruvate (i) (n = 3 biological independent samples). (j) Mass isotopologue analysis of [U-^{13}C] pyruvate-traced citrate in control and *YBX1* knockdown MDA-MB-231 cells with or without glutamine treatment (n = 3 biological independent samples).

for 48 h. Next, after recovering for another 24 h (without puromycin), cells were seeded in 96-well plates with an average number of 50 cells per well to obtain the single-cell colony. After colonies formed, colonies with a knockout of target genes were identified by western blotting and DNA sequencing.

In vivo animal studies

Ybx1$^{fl/fl}$ mice were generated and obtained from GemPharmatech. Male BALB/c nude mice (6–8 weeks old) were obtained from Dalian Medical University and maintained under specific pathogen-free conditions. For tumor growth assay, MHCC-97H cells (1×10^6 per mice) in 100 μL of cell suspension (mixed with Matrigel at a 1:1 ratio) were injected subcutaneously. The tumors were removed, photographed, and weighed 5 weeks after injection. For tumor lung metastasis assay, MHCC-97H cells (2×10^6 per mice) in 150 μL phosphate-buffered saline (PBS) were injected into the tail vein. The lungs were removed and photographed followed by nodules counting. Hematoxylin and eosin (H&E) staining was carried out using the H&E staining kit (Yuan Ye Biotech, R20570) according to the manufacturer's instructions. All experiments were carried out according to the regulations set by the Ethics Committee of Dalian Medical University.

Immunoblotting and co-immunoprecipitation

Cells were harvested and proteins were extracted using ice-cold lysis buffer (150 mmol/L NaCl, 1% Triton X-100, 1 mmol/L ethylenediaminetetraacetic acid [EDTA], 1 mmol/L ethylene glycol-bis(2-aminoethyl ether)-N,N,N',N'-tetraacetic acid [EGTA], 2.5 mmol/L sodium pyrophosphate, 1 mmol/L β-glycerolphosphate, 20 mmol/L Tris-HCl, pH 7.5, with protease inhibitor cocktail). For histone and histone lactylation detection, cells were extracted using lysis buffer supplemented with 0.5% sodium dodecyl sulfate (SDS) followed by appropriate sonification. For immunoprecipitation, proteins were extracted from cells or isolated mitochondria using ice-cold octyl-β-D-glucopyranoside (ODG) lysis buffer (2% ODG, 100 mmol/L NaCl, 50 mmol/L Tris-HCl, pH 8.0, 1 mmol/L EDTA, 1 mmol/L EGTA, 5 mmol/L β-mercaptoethanol with protease inhibitor cocktail) followed by sonification on ice 10–15 times (per 2 s at once, avoid protein denaturation). Cell lysates were precleared by incubating with protein A/G magnetic beads for 1 h, and then incubated with the respective antibodies overnight. The next day, appropriate A/G magnetic beads were added to the lysates and mixed for 2 h. The beads were washed using ODG buffer four times (per 10 min at once) at 4°C and then denatured using 2× SDS sample buffer and subjected to western blot analysis.

For immunoprecipitation purification of native FLAG-tagged MPC1 and YBX1 complex, HEK 293T cells were transfected with control plasmid or C-terminal S-protein-FLAG-tagged MPC1. After 48 h transfection, cells were subjected to mitochondria isolation described below. Mitochondria were lysed with native lysis buffer (4% (w/v) digitonin, 50 mmol/L NaCl, 50 mmol/L imidazole/HCl (pH 7.0), 2 mmol/L 6-aminohexanoic acid, 1 mmol/L EDTA) in a final concentration of 6 mg protein/mL. After spinning at 20,000 *g* at 4°C for 20 min, the supernatant was incubated with anti-FLAG beads for 4 h at 4°C. The immunoprecipitation beads were washed with washing native lysis buffer adjusted digitonin to 0.2% three times. Immunoprecipitated proteins were eluted by washing native lysis buffer containing 400 μg/mL FLAG peptide and 10% glycerol. Blue native PAGE was performed as described previously [59].

Sample preparation for IP-MS and database searching

Mitochondria used for IP-MS were isolated as described below. Flag beads-precipitated proteins of YBX1 or control vector were subjected to digestion as described previously [60]. Briefly, precipitates were dissolved using washing buffer 1 (8 mol/L urea and 100 mmol/L NH_4HCO_3). Solutions were loaded in a 10 kDa ultrafiltration centrifugal tube and spun down at 12,000 *g* for 30 min. The precipitates were then washed with 400 μL washing buffer 1 twice, and redissolved in washing buffer 1 containing 5 mmol/L tris(2-carboxyethyl)phosphine at 25°C for 30 min. Proteins were alkylated by 10 mmol/L iodoacetic acid for 30 min, followed by centrifuging at 12,000 *g* for 30 min. Then, precipitates were washed with washing buffer 2 (20 mmol/L NH_4HCO_3) three times. Proteins were digested with trypsin/protein (1:20, (w/w)) overnight at 37°C. After digestion, 10% formic acid (FA) was added to adjust pH to 3.0 to stop the reaction, and the peptide mixture was obtained by centrifuging at 12,000 *g* for 30 min. The peptide mixture was vacuum freeze-dried at 45°C and redissolved in 0.1% FA before performed on nanoLC-MS/MS. Spectra were recorded on a ZenoTOF 7600 mass spectrometer (SCIEX) and MaxQuant [61] software suit (version 2.2.0.0) was used for mass spectrometry data searching and data analysis.

Cell growth measurement

Cell proliferation was performed by cell counting kit-8 (CCK-8) assay according to the manufacturer's requirement. Briefly, indicated cells (1000–2000 per well) were seeded in a 96-well plate. At different time points (24 h for a time point, total five time points), cells were incubated with a 100 μL relative culture medium containing 10% CCK-8 assay solution. After 2 h of incubation, plates were measured at 450 nm using a plate reader (Cytation5, Biotech). For growth assay under treatment with different concentrations of UK5099, 3000 cells were plated in 96-well and CCK-8 assay was performed to determine the initial cell numbers after attachment for 24 h. At the same time, the rest of the wells on the plate were changed in a medium containing different concentrations of UK5099. After 48 h of incubation, cell numbers were determined by using CCK-8.

Transwell invasion assay

Cells (5×10^4 for MDA-MB-231 cells, and 1×10^5 for MHCC-97H cells) were seeded in the Matrigel pre-coated chambers in a 200 μL medium without serum. The lower chamber was added 500 μL medium with 15% FBS as a chemoattractant. After incubation (12 h for MDA-MB-231 cells, 36 h for MHCC-97H cells), cells were fixed and stained with 0.1% crystal violet solution containing 10% methanol for 10 min. Cells that did not cross the membrane pores were cleaned with a cotton swab, and the rest cells were pictured and counted.

Gln, glutamine (2 mmol/L). (k) Mass isotopologue analysis of [U-^{13}C] glucose-traced pyruvate in *MPC1*$^{-/-}$ MDA-MB-231 cells transduced with control or *YBX1* shRNA (n = 3 biological independent samples). (l) Immunoblotting of YBX1, Pan Kla (histone lactylation), and Histone H3 in MDA-MB-231 and MHCC-97H cells transduced with control or *YBX1* shRNA with or without 20 μmol/L UK5099 treatment. Results are the mean of biological replicates from a representative experiment, and error bars indicate SD. Statistical significance was determined by a two-tailed, unpaired Student's *t*-test. All other experiments were repeated independently at least three times.

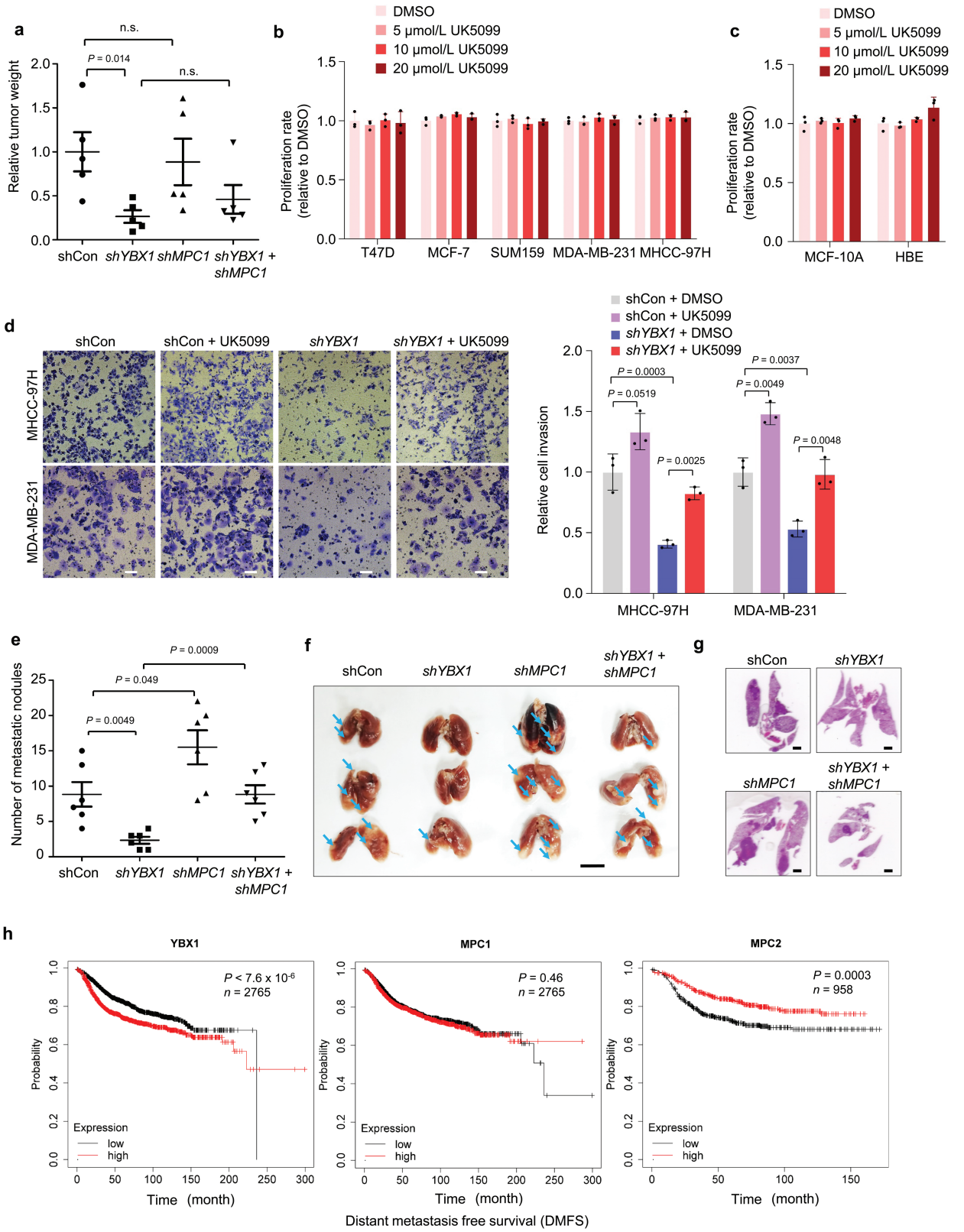

Figure 5 YBX1 promotes cancer cell metastasis by inhibiting the MPC complex. (a) Xenograft tumor weight (relative to control). Mice were injected subcutaneously with MHCC-97H cells transduced with *YBX1* shRNA alone or in combination with *MPC1* shRNA (n = 5 tumors for each group). (b and c) Proliferation assay of indicated cell lines treated with vehicle or different concentrations of UK5099 (n = 3 biological independent samples). (d) Representative images (left panel) and data quantification (right panel) of transwell invasion assay by MHCC-97H and MDA-MB-231 cells transduced with *YBX1* shRNA under 20 μmol/L UK5099 treatment (n= 4 biological independent samples). Scale bar, 100 μm. (e–g) Number of metastatic nodules (e), bright-field imaging. Scale bar, 1 cm. (f), and H&E staining of the lungs with tail vein injected MHCC-97H cells transduced with *YBX1* shRNA alone or in combination with *MPC1* shRNA (g) (n = 6 biological independent samples). Scale bar, 200 mm. (h) Kaplan–Meier curves of distant metastasis-free survival times of breast cancer patients, stratified by *YBX1*, *MPC1*, or *MPC2* expression. Data were obtained from the website of Kaplan–Meier Plotter online. Results are the mean of biological replicates from a representative experiment, and error bars indicate SD. Statistical significance was determined by a two-tailed, unpaired Student's *t*-test. The experiments in (b), (c), and (d) were performed independently at least three times.

Confocal microscopy and structured illumination microscopy

For confocal microscopy, cells (1×10^4) that stably expressed C-terminal fused Ha-tagged MPC1 or MPC2 were seeded in confocal dishes (Biofilm) for 48 h. The cells were then fixed with 4% paraformaldehyde diluted in PBS for 15 min at room temperature. After being washed with PBS three times, cells were incubated with blocking buffer containing 0.3% triton X-100 for 60 min, and then incubated with anti-PDHA1 antibody (1:50, Santa Cruz, sc-377092), anti-YBX1 antibody (1:400, Abcam, ab12148), anti-FLAG antibody (1:200, Sigma, F1804), and anti-HA antibody (1:200, Santa Cruz, sc-7392) at 4°C overnight. Cells were then washed with PBS three times and incubated with Alexa Fluor 488-conjugated anti-mouse secondary antibody and Alexa Fluor 555-conjugated anti-rabbit secondary antibody for 2 h at room temperature followed by incubation with 4′-6-diamidino-2-phenylindole (DAPI) for 5 min. Confocal images were acquired under a Yokogawa Spinning Disk Field Scanning Confocal System using 100× oil immersion objective lens, 1.49 NA (Nikon).

For structured illumination microscopy, cells were treated following the same protocols of confocal microscopy as described above. Super-resolution images were taken on a Nikon N-SIM (structured illumination microscopy, a microscopy technique) system with a 100× oil immersion objective lens, 1.49 NA (Nikon). Images were captured using Nikon Imaging Software (NIS)-Elements and reconstructed using slice reconstruction in NIS-Elements. Excitation: 488 nm, collected: 500–545 nm (green channel). Excitation: 555 nm, collected: 570–640 nm (red channel).

Immuno-electron microscopy

The fixation condition for the polyclonal anti-YBX1 antibody (1:400, Abcam, ab12148) in Immuno-EM assay was pretested using immunofluorescence assays. Control and *YBX1*$^{-/-}$ MDA-MB-231 cells were fixed with PB buffer (0.1 mol/L Na_2HPO_4:0.1 mol/L NaH_2PO_4 = 81:19, in water, pH 7.4) containing 4% formaldehyde and 0.1% glutaraldehyde at 4°C overnight. Samples were hydrated by ethanol and embedded in London Resin-White resin for more than 48 h at –20°C. Embedded cells were cut into 70 nm sections on the ultra-microtome. The sections were blocked with 1% bovine serum albumin (BSA) in tris-buffered saline (TBS) buffer for 30 min at room temperature and followed by incubated with polyclonal anti-YBX1 antibody (1:10, Abcam, ab12148) in 1% BSA TBS solution overnight at 4°C. After washed with TBS solution three times, sections were incubated with 12 nm colloidal gold-labeled rabbit secondary antibody (1:25, Jackson ImmunoResearch, 111-205-144) for 2 h at room temperature. After washed with TBS solution five times, grids were stained with 2% uranium acetate for 8 min. Sections were viewed and pictured using HITACHI HT7800 transmission electron microscope (80 kV).

OCR measurement

Cells (MDA-MB-231 for 1.5×10^4 cells per well, MCF-7 for 2×10^4 cells per well, and MEFs for 2.5×10^4 cells per well) were plated in a 24-well plate (Agilent Technologies). The OCR measurement was performed with an XFe24 extracellular flux analyzer (Agilent Technologies) according to the manufacturer's instructions. The XF DMEM measurement medium was supplemented with 2 mmol/L glutamine, 10 mmol/L glucose, and 2 mmol/L pyruvate. The compounds used in the assay were oligomycin (2 μmol/L), carbonyl cyanide *p*-trifluoromethoxyphenylhydrazone (FCCP) (0.75 μmol/L), and rotenone (0.5 μmol/L)/antimycin A (0.5 μmol/L).

BRET-based MPC activity assay

MPC BRET assay was performed as described previously [13]. Briefly, cells were stably transfected with MPC1-Venus and MPC2-Rluc using lentivirus infection. Cells (20,000 cells per well) were seeded in white 96-well plates. After cell attachment for 24 h, cells were washed twice with the 37°C pre-warmed PBS containing 1 mmol/L $CaCl_2$ and 0.5 mmol/L $MgCl_2$. Signals were obtained after adding 5 μmol/L coelenterazine h (Invitrogen, C6780) followed by the addition of 5 mmol/L pyruvate, and the absorbance was measured using the plate reader (filter for Rluc, 485 ± 20 nm, filter for Venus, 528 ± 20 nm, Cytation5, Biotech). BRET value was defined as the emission at 528 nm/485 nm.

Gas chromatography-mass spectrometry-based metabolite analysis and stable isotope tracing *in vivo* and *in vitro*

For untargeted metabolite measurement, cells were changed to the fresh medium and incubated for 24 h. After incubation, cells were washed with ice-cold PBS three times and frozen with liquid nitrogen. Extracellular metabolites were tested by using 70 μL of incubated medium. [U-^{13}C] glucose, [U-^{13}C] pyruvate, and [U-^{13}C] glutamine were purchased from Cambridge Isotope Laboratories. For the cultured cell tracing experiment, [U-^{13}C] glucose (25 mmol/L), [U-^{13}C] pyruvate (2 mmol/L), or [U-^{13}C] glutamine (2 mmol/L) was used to substitute the relative metabolite in DMEM (no glucose, no glutamine, no pyruvate, and no phenol-red) containing 10% dialyzed FBS, and the rest metabolites were unlabeled. After the tracing experiment, cells were washed with cold PBS three times and frozen in liquid nitrogen. Sample preparation and methods of metabolomics analysis were performed as described previously [62]. Natural isotope abundance was corrected using IsoCor v.2.0 [63].

Subcellular mitochondria fractionation

Mitochondria were isolated from cells as described previously [64, 65] with some modifications. Briefly, cells were washed twice with potassium phosphate-buffered saline (KPBS, 136 mmol/L KCl, 10 mmol/L KH_2PO_4, pH 7.2 adjusted using KOH) and then scraped to 15 mL polypropylene Falcon tubes using KPBS. Cells were centrifuged at 600 *g* at 4°C for 4 min, and then the supernatant was discarded and the pellet was suspended with isolation buffer (10 mmol/L 3-(N-Morpholino)propanesulfonic acid [Tris-MOPS], pH 7.4, 1 mmol/L EGTA, 0.2 mol/L sucrose). Cells were homogenized with 50–60 strokes using a glass Dounce homogenizer, and then the homogenate solution was transferred to a new tube and centrifuged at 600 *g* at 4°C for 10 min. The supernatant was spun down at 7000 *g* at 4°C for 10 min. The residual supernatant was kept as cytosolic fractions, and the pellet was the intact mitochondria which were washed with isolation buffer twice and immediately subjected to the follow-up experiment. For nuclear fractions, cells were suspended in hypotonic buffer solution (10 mmol/L NaCl, 3 mmol/L $MgCl_2$, 20 mmol/L Tris-HCl, pH 7.4) on ice for 15 min, and then, 0.05% NP40 was added and vortexed immediately for 15 s. Subsequently, the nuclear fractions were pelleted by spun down at 1000 *g* at 4°C for 10 min. Finally, the pellet was washed with PBS twice and subjected to western blot analysis.

For the PK resistance assay, freshly isolated mitochondria were re-suspended with isolation buffer at 1 mg/mL and equally

divided into 50 μL per tube on ice. The disruption of mitochondrial outer membrane was performed with 50 μL osmotic buffer (10 mmol/L KH_2PO_4, pH 7.4). PK (0.5–200 μg/mL) was added to the aliquots of mitochondria on ice for 30 min. Subsequently, 2 mmol/L PMSF was added to inactivate the protease for 5 min followed by mixing with 2 × SDS loading buffer.

To analyze the interaction between YBX1 and the mitochondrial membrane, 200 μg isolated mitochondria was suspended with isolation buffer or 0.1 mol/L sodium carbonate (pH 10.5, 11, or 11.5) on ice for 1 h, and the suspension was agitated once every 10 min. Membranes were obtained at 45,000 *g* at 4°C for 1 h. For sonication, 200 μg isolated mitochondria was sonicated on ice for 3 min, and the membrane was pelleted at 45,000 *g* at 4°C for 1 h. The pellets (P) were kept for the follow-up analysis. All the supernatant was precipitated with 12% trichloroacetic acid (TCA) for 10 min on ice and washed with ice-cold acetone five times on a sonication incubator to remove the residual TCA, and the precipitates from the supernatant and pellets from the membrane were dissolved in SDS sample buffer for western blot analysis.

Mitochondria isotope tracing

Mitochondria $^{13}C_3$ pyruvate tracing was performed as described previously with minor modifications [66]. Fresh mitochondria pellets were incubated in 300 μL tracing buffer A (120 mmol/L KCl, 5 mmol/L KH_2PO_4, 1 mmol/L EGTA, 10 mmol/L Tris-MOPS, pH 7.4), and [U-^{13}C] pyruvate tracing was initiated by adding 600 μL tracing buffer B (0.15 mmol/L [U-^{13}C] pyruvate, 0.075 mmol/L malate, 120 mmol/L KCl, 5 mmol/L KH_2PO_4, 1 mmol/L EGTA, 10 mmol/L Tris-MOPS, pH 6.8). Isotope tracing was performed at room temperature in a rotator for the indicated time. When the tracing assay finished, MPC inhibitor UK5099 (10 μmol/L) was added and the mitochondria suspension was centrifuged at 10,000 *g* at 4°C for 1 min. The supernatant was discarded, and the mitochondria pellets were washed with ice-cold KPBS containing 10 μmol/L UK5099 and subjected to centrifuging at 10,000 *g* at 4°C for 1 min. The mitochondrial metabolites were extracted, prepared, and measured as described above.

Mitochondrial pyruvate uptake assay

Mitochondrial pyruvate uptake detection was performed using the inhibitor-stop based on the gas chromatography-mass spectrometry (GC-MS) method. Briefly, an equal amount of mitochondria were incubated in uptake buffer (120 mmol/L KCl, 5 mmol/L KH_2PO_4, 1 mmol/L EGTA, 3 mmol/L 4-(2-hydroxyethyl)piperazine-1-ethanesulfonic acid [HEPES], pH 7.4) and transferred to twice volumes of the uptake buffer (pH 6.8) supplemented with 0.075 mmol/L malate and 0.15 mmol/L [U-^{13}C] pyruvate to initiate the import for 10 min at room temperature. After pyruvate uptake, UK5099 (10 μmol/L) was added and mixed, followed by centrifugation at 10,000 *g* at 4 °C for 1 min. One hundred microliters of supernatant was transferred to 500 μL methanol/water (4:1, (v/v), containing 20 μmol/L unlabeled pyruvate as an internal standard) and centrifuged at 10,000 *g* at 4 °C for 5 min. The supernatant was dried down for further GC-MS sample preparation followed by GC-MS analysis. The levels of mitochondrial pyruvate uptake were defined as subtracting the level of remaining pyruvate in the supernatant from the starting amount of pyruvate.

Statistical analysis

Data were processed using GraphPad Prism version 5.0 (GraphPad Software, San Diego, CA) and presented as mean ± SD. Two-tailed unpaired Student's *t*-test (normal distribution) was used to assess significance between two groups. $P < 0.05$ was considered statistically significant.

Supplementary data

Supplementary material is available at *Life Metabolism* online.

Acknowledgements

We thank members of Dr. Piao laboratory for the helpful discussion. We also thank Dr. Guowang Xu for providing GC-MS-based metabolic assay system.

Author contributions

H.L.P. and H.C. conceived the project, and H.L.P. supervised the project. H.C. and H.L.P. designed the project and H.C. performed most of the experiments, D.C. performed computational data analysis, F.W. provided guidance on phosphorylation proteomics analysis method, J.C.M. provided MPC1/2 BRET system plasmids, and W.L. performed the SIM microscopy analysis under the guidance of Z.X.. H.C., D.C., and H.L.P. analyzed data. T.L., H.Q., T.X., X.L., W.W., X.G., W.O., F.W., Z.X., and J.C.M. provided significant intellectual input. H.C. and H.L.P. wrote the manuscript with input from all other authors.

Conflict of interest

The authors declare that no conflict of interest exists.

Funding

This study was supported by the National Key Research and Development Program of China (2022YFA0806503), grants from the National Natural Science Foundation of China (No. 81972625, No. 21907093), Dalian Science and Technology Innovation Funding (2019J12SN52), Liaoning Revitalization Talents Program (XLYC2002035).

Ethics approval

All procedures were performed in accordance with the Ethics Committee of Dalian Medical University.

Data availability

All study data are included in the article and/or supplementary information. Materials are available upon request.

References

1. Jeoung NH, Harris CR, Harris RA. Regulation of pyruvate metabolism in metabolic-related diseases. *Rev Endocr Metab Disord* 2014;**15**:99–110.
2. Olson KA, Schell JC, Rutter J. Pyruvate and metabolic flexibility: illuminating a path toward selective cancer therapies. *Trends Biochem Sci* 2016;**41**:219–30.
3. Koppenol WH, Bounds PL, Dang CV. Otto Warburg's contributions to current concepts of cancer metabolism. *Nat Rev Cancer* 2011;**11**:325–37.

4. Luengo A, Li Z, Gui DY *et al*. Increased demand for NAD^+ relative to ATP drives aerobic glycolysis. *Mol Cell* 2021;**81**:691–707.e6.
5. Bricker DK, Taylor EB, Schell JC *et al*. A mitochondrial pyruvate carrier required for pyruvate uptake in yeast, *Drosophila*, and humans. *Science* 2012;**337**:96–100.
6. Herzig S, Raemy E, Montessuit S *et al*. Identification and functional expression of the mitochondrial pyruvate carrier. *Science* 2012;**337**:93–6.
7. Schell JC, Olson KA, Jiang L *et al*. A role for the mitochondrial pyruvate carrier as a repressor of the Warburg effect and colon cancer cell growth. *Mol Cell* 2014;**56**:400–13.
8. Flores A, Schell J, Krall AS *et al*. Lactate dehydrogenase activity drives hair follicle stem cell activation. *Nat Cell Biol* 2017;**19**:1017–26.
9. Schell JC, Wisidagama DR, Bensard C *et al*. Control of intestinal stem cell function and proliferation by mitochondrial pyruvate metabolism. *Nat Cell Biol* 2017;**19**:1027–36.
10. Kim J, Yu L, Chen W *et al*. Wild-type p53 promotes cancer metabolic switch by inducing PUMA-dependent suppression of oxidative phosphorylation. *Cancer Cell* 2019;**35**:191–203.e8.
11. Vanderperre B, Cermakova K, Escoffier J *et al*. MPC1-like is a placental mammal-specific mitochondrial pyruvate carrier subunit expressed in postmeiotic male germ cells. *J Biol Chem* 2016;**291**:16448–61.
12. Zangari J, Petrelli F, Maillot B *et al*. The multifaceted pyruvate metabolism: role of the mitochondrial pyruvate carrier. *Biomolecules* 2020;**10**:1068.
13. Compan V, Pierredon S, Vanderperre B *et al*. Monitoring mitochondrial pyruvate carrier activity in real time using a BRET-based biosensor: investigation of the Warburg effect. *Mol Cell* 2015;**59**:491–501.
14. Bensard CL, Wisidagama DR, Olson KA *et al*. Regulation of tumor initiation by the mitochondrial pyruvate carrier. *Cell Metab* 2020;**31**:284–300.e7.
15. Muthusamy T, Cordes T, Handzlik MK *et al*. Serine restriction alters sphingolipid diversity to constrain tumour growth. *Nature* 2020;**586**:790–5.
16. Liu X, Chen D, Chen H *et al*. YB1 regulates miR-205/200b-ZEB1 axis by inhibiting microRNA maturation in hepatocellular carcinoma. *Cancer Commun (Lond)* 2021;**41**:576–95.
17. Chen X, Li A, Sun BF *et al*. 5-methylcytosine promotes pathogenesis of bladder cancer through stabilizing mRNAs. *Nat Cell Biol* 2019;**21**:978–90.
18. El-Naggar AM, Veinotte CJ, Cheng H *et al*. Translational activation of HIF1α by YB-1 promotes sarcoma metastasis. *Cancer Cell* 2015;**27**:682–97.
19. Coles LS, Lambrusco L, Burrows J *et al*. Phosphorylation of cold shock domain/Y-box proteins by ERK2 and GSK3β and repression of the human VEGF promoter. *FEBS Lett* 2005;**579**:5372–8.
20. Lu ZH, Books JT, Ley TJ. YB-1 is important for late-stage embryonic development, optimal cellular stress responses, and the prevention of premature senescence. *Mol Cell Biol* 2005;**25**:4625–37.
21. Jayavelu AK, Schnöder TM, Perner F *et al*. Splicing factor YBX1 mediates persistence of *JAK2*-mutated neoplasms. *Nature* 2020;**588**:157–63.
22. Evdokimova V, Tognon C, Ng T *et al*. Translational activation of snail1 and other developmentally regulated transcription factors by YB-1 promotes an epithelial-mesenchymal transition. *Cancer Cell* 2009;**15**:402–15.
23. Rabiee A, Plucińska K, Isidor MS *et al*. White adipose remodeling during browning in mice involves YBX1 to drive thermogenic commitment. *Mol Metab* 2021;**44**:101137.
24. Xu L, Li H, Wu L *et al*. YBX1 promotes tumor growth by elevating glycolysis in human bladder cancer. *Oncotarget* 2017;**8**:65946–56.
25. de Souza-Pinto NC, Mason PA, Hashiguchi K *et al*. Novel DNA mismatch-repair activity involving YB-1 in human mitochondria. *DNA Repair (Amst)* 2009;**8**:704–19.
26. Jady BE, Ketele A, Kiss T. Dynamic association of human mRNP proteins with mitochondrial tRNAs in the cytosol. *RNA* 2018;**24**:1706–20.
27. Matsumoto S, Uchiumi T, Saito T *et al*. Localization of mRNAs encoding human mitochondrial oxidative phosphorylation proteins. *Mitochondrion* 2012;**12**:391–8.
28. Cho NH, Cheveralls KC, Brunner AD *et al*. OpenCell: endogenous tagging for the cartography of human cellular organization. *Science* 2022;**375**:eabi6983.
29. Huttlin EL, Bruckner RJ, Navarrete-Perea J *et al*. Dual proteome-scale networks reveal cell-specific remodeling of the human interactome. *Cell* 2021;**184**:3022–40.e28.
30. van Roeyen CR, Scurt FG, Brandt S *et al*. Cold shock Y-box protein-1 proteolysis autoregulates its transcriptional activities. *Cell Commun Signal* 2013;**11**:63.
31. Dietmair S, Hodson MP, Quek LE *et al*. A multi-omics analysis of recombinant protein production in Hek293 cells. *PLoS One* 2012;**7**:e43394.
32. Henry O, Jolicoeur M, Kamen A. Unraveling the metabolism of HEK-293 cells using lactate isotopomer analysis. *Bioprocess Biosyst Eng* 2011;**34**:263–73.
33. Buescher JM, Antoniewicz MR, Boros LG *et al*. A roadmap for interpreting ^{13}C metabolite labeling patterns from cells. *Curr Opin Biotechnol* 2015;**34**:189–201.
34. Boese AC, Kang S. Mitochondrial metabolism-mediated redox regulation in cancer progression. *Redox Biol* 2021;**42**:101870.
35. Yang L, Venneti S, Nagrath D. Glutaminolysis: a hallmark of cancer metabolism. *Annu Rev Biomed Eng* 2017;**19**:163–94.
36. Vacanti NM, Divakaruni AS, Green CR *et al*. Regulation of substrate utilization by the mitochondrial pyruvate carrier. *Mol Cell* 2014;**56**:425–35.
37. Yang C, Ko B, Hensley CT *et al*. Glutamine oxidation maintains the TCA cycle and cell survival during impaired mitochondrial pyruvate transport. *Mol Cell* 2014;**56**:414–24.
38. Gao P, Tchernyshyov I, Chang TC *et al*. c-Myc suppression of miR-23a/b enhances mitochondrial glutaminase expression and glutamine metabolism. *Nature* 2009;**458**:762–5.
39. Wise DR, DeBerardinis RJ, Mancuso A *et al*. Myc regulates a transcriptional program that stimulates mitochondrial glutaminolysis and leads to glutamine addiction. *Proc Natl Acad Sci U S A* 2008;**105**:18782–7.
40. Feng M, Xie X, Han G *et al*. YBX1 is required for maintaining myeloid leukemia cell survival by regulating BCL2 stability in an m^6A-dependent manner. *Blood* 2021;**138**:71–85.
41. Liu S, Marneth AE, Alexe G *et al*. The kinases IKBKE and TBK1 regulate MYC-dependent survival pathways through YB-1 in AML and are targets for therapy. *Blood Adv* 2018;**2**:3428–42.
42. Bommert KS, Effenberger M, Leich E *et al*. The feed-forward loop between YB-1 and MYC is essential for multiple myeloma cell survival. *Leukemia* 2013;**27**:441–50.
43. Bott AJ, Peng IC, Fan Y *et al*. Oncogenic Myc induces expression of glutamine synthetase through promoter demethylation. *Cell Metab* 2015;**22**:1068–77.
44. Dichtl S, Lindenthal L, Zeitler L *et al*. Lactate and IL6 define separable paths of inflammatory metabolic adaptation. *Sci Adv* 2021;**7**:eabg3505.

45. Zhang D, Tang Z, Huang H *et al*. Metabolic regulation of gene expression by histone lactylation. *Nature* 2019;**574**:575–80.
46. Takaoka Y, Konno M, Koseki J *et al*. Mitochondrial pyruvate carrier 1 expression controls cancer epithelial-mesenchymal transition and radioresistance. *Cancer Sci* 2019;**110**:1331–9.
47. Ohashi T, Eguchi H, Kawamoto K *et al*. Mitochondrial pyruvate carrier modulates the epithelial-mesenchymal transition in cholangiocarcinoma. *Oncol Rep* 2018;**39**:1276–82.
48. Ha B, Lee EB, Cui J *et al*. YB-1 overexpression promotes a TGF-β1-induced epithelial-mesenchymal transition via Akt activation. *Biochem Biophys Res Commun* 2015;**458**:347–51.
49. Matsumoto S, Uchiumi T, Tanamachi H *et al*. Ribonucleoprotein Y-box-binding protein-1 regulates mitochondrial oxidative phosphorylation (OXPHOS) protein expression after serum stimulation through binding to OXPHOS mRNA. *Biochem J* 2012;**443**:573–84.
50. Rath S, Sharma R, Gupta R *et al*. MitoCarta3.0: an updated mitochondrial proteome now with sub-organelle localization and pathway annotations. *Nucleic Acids Res* 2021;**49**:D1541–7.
51. Jobard E, Pontoizeau C, Blaise BJ *et al*. A serum nuclear magnetic resonance-based metabolomic signature of advanced metastatic human breast cancer. *Cancer Lett* 2014;**343**:33–41.
52. Torrino S, Grasset EM, Audebert S *et al*. Mechano-induced cell metabolism promotes microtubule glutamylation to force metastasis. *Cell Metab* 2021;**33**:1342–57.e10.
53. Bergers G, Fendt SM. The metabolism of cancer cells during metastasis. *Nat Rev Cancer* 2021;**21**:162–80.
54. Najumudeen AK, Ceteci F, Fey SK *et al*. The amino acid transporter SLC7A5 is required for efficient growth of KRAS-mutant colorectal cancer. *Nat Genet* 2021;**53**:16–26.
55. Tasdogan A, Faubert B, Ramesh V *et al*. Metabolic heterogeneity confers differences in melanoma metastatic potential. *Nature* 2020;**577**:115–20.
56. Chen P, Zuo H, Xiong H *et al*. Gpr132 sensing of lactate mediates tumor-macrophage interplay to promote breast cancer metastasis. *Proc Natl Acad Sci U S A* 2017;**114**:580–5.
57. Collot M, Wattiaux-De Coninck S, Wattiaux R. Deterioration of rat-liver mitochondria during isopycnic centrifugation in an isoosmotic medium. *Eur J Biochem* 1975;**51**:603–8.
58. Machado AM, Desler C, Bøggild S *et al*. *Helicobacter pylori* infection affects mitochondrial function and DNA repair, thus, mediating genetic instability in gastric cells. *Mech Ageing Dev* 2013;**134**:460–6.
59. Wittig I, Braun HP, Schagger H. Blue native PAGE. *Nat Protoc* 2006;**1**:418–28.
60. Liu Z, Yang S, Zhou L *et al*. Structural characterization of protein-material interfacial interactions using lysine reactivity profiling-mass spectrometry. *Nat Protoc* 2023;**18**:2600–23.
61. Cox J, Mann M. MaxQuant enables high peptide identification rates, individualized p.p.b.-range mass accuracies, and proteome-wide protein quantification. *Nat Biotechnol* 2008;**26**:1367–72.
62. Yan M, Qi H, Xia T *et al*. Metabolomics profiling of metformin-mediated metabolic reprogramming bypassing AMPKα. *Metabolism* 2019;**91**:18–29.
63. Millard P, Delépine B, Guionnet M *et al*. IsoCor: isotope correction for high-resolution MS labeling experiments. *Bioinformatics* 2019;**35**:4484–7.
64. Frezza C, Cipolat S, Scorrano L. Organelle isolation: functional mitochondria from mouse liver, muscle, and cultured fibroblasts. *Nat Protoc* 2007;**2**:287–95.
65. Chen WW, Freinkman E, Wang T *et al*. Absolute quantification of matrix metabolites reveals the dynamics of mitochondrial metabolism. *Cell* 2016;**166**:1324–37.e11.
66. Yang C, Ko B, Hensley CT *et al*. Glutamine oxidation maintains the TCA cycle and cell survival during impaired mitochondrial pyruvate transport. *Mol Cell* 2014;**56**:414–24.